

# A Kernel-free Boundary Integral Method for the Bidomain Equations

Xindan Gao, Li Cai, Craig S. Henriquez and Wenjun Ying

School of Mathematical Sciences and Institute of Natural Sciences, Shanghai Jiao Tong University, Shanghai, China

**Abstract.** The bidomain equations have been widely used to mathematically model the electrical activity of the cardiac tissue. In this work, we present a potential theory-based Cartesian grid method which is referred as the kernel-free boundary integral (KFBI) method which works well on complex domains to efficiently simulate the linear diffusion part of the bidomain equation. After a proper temporal discretization, the KFBI method is applied to solve the resulting homogeneous Neumann boundary value problems with a second-order accuracy. According to the potential theory, the boundary integral equations reformulated from the boundary value problems can be solved iteratively with the simple Richardson iteration or the Krylov subspace iteration method. During the iteration, the boundary and volume integrals are evaluated by limiting the structured grid-based discrete solutions of the equivalent interface problems at quasi-uniform interface nodes without the need to know the analytical expression of Green's functions. In particular, the discrete linear system of the equivalent interface problem obtained from the standard finite difference schemes or the finite element schemes can be efficiently solved by fast elliptic solvers such as the fast Fourier transform based solvers or those based on geometric multigrid iterations after an appropriate modification at the irregular grid nodes. Numerical results for solving the FitzHugh-Nagumo bidomain equations in both two- and three-dimensional spaces are presented to demonstrate the numerical performance of the KFBI method such as the second-order accuracy and the propagation and scroll wave of the voltage simulated on the real human left ventricle model.

**Keywords** Bidomain equations; Strang splitting; Cartesian grid method; Kernel-free boundary integral method; FFT; GMRES iteration

## 1 Introduction

The set of bidomain equations, consisting of the equations for the intra- and extracellular potentials, is currently the most complete mathematical model for describing the electrical activities of the cardiac tissue [1]. The cardiac simulations are inherently computationally expensive on account of several factors such as the high resolution in space and time discretization and the high complexity of living systems. To be specific, the numerical computational time is mainly consumed in a burdensome part resulting from the linear system discretized from the bidomain equations which should be solved repeatedly [2].

In detailed numerical simulations, for the temporal discretization, the explicit methods such as the forward Euler method and Runge Kutta method are the easiest way to implement. Although they do not require matrix inversion, the timesteps allowed in these methods are generally very small to satisfy the requirement of stability [3–5]. The fully implicit methods, preferred for stiff systems, have no timestep restriction, but they often have the significant drawback of requiring the numerical solution of a very large-scale nonlinear system at each timestep [6–8]. The semi-implicit method combines the advantages of the above methods that it allows for a much larger timestep than that used in the explicit method and requires the numerical solution of a linear system at each timestep [9]. Operator splitting such as the first-order Godunov splitting and the second-order Strang splitting is a popular technique being able to

uncouple the cell-model ordinary differential equation (ODE) system from the electro-diffusive parts of the bidomain equations [9–12]. In this work, the second-order Strang splitting is applied to split the bidomain equations into two manageable parts, *i.e.*, the nonlinear reaction and linear diffusion parts.

For the spatial discretization of the domain, the finite difference method (FDM) [1, 13, 14] is usually applied to solve the bidomain equations on a regular computational space, but it lacks the ability to follow complex surfaces. Although the finite element method (FEM) [15–17] and the finite volume method (FVM) [18, 19] have the advantages of being able to model boundary conditions at the curved surfaces of the heart, they are generally more difficult to implement and more computationally expensive than the FDM.

In our implementation, after applying the second-order Strang splitting to decouple the bidomain equations into the nonlinear reaction and linear diffusion parts, we discrete the nonlinear reaction part by the forward Euler method in the first half step and by the backward Euler method in the second half step. The resulting discrete nonlinear systems are space independent which can be solved efficiently. We integrate the linear diffusion part by the second-order mid-point method where the obtained semi-discrete equation is a coupled elliptic system with a possible anisotropy. In this work, we present an accurate and efficient algorithm, a generalized boundary integral method, to solve the semi-discrete diffusion part of the bidomain equations, *i.e.*, the so-called kernel-free boundary integral (KFBI) method. As a direct extension of the grid-based boundary method by Mayo [20–22], the KFBI method proposed by Ying *et.al.* [23, 24] can efficiently solve the variable coefficients elliptic partial differential equations (PDE) with possible anisotropy and inhomogeneity.

When solving the coupled semi-discrete diffusion system with a Neumann boundary condition by the KFBI method with second-order accuracy, we first reformulate the system as the boundary integral equations (BIEs) where the density defined on the domain boundary is unknown. The BIEs then can be iteratively solved with a Krylov subspace iteration method such as the generalized minimal residual (GMRES) [25] iteration or the simple Richardson iteration. During the iteration, the boundary and volume integrals can be evaluated by computing the limit values of the structured grid-based numerical solutions of the equivalent interface problem without the need to know the analytical expressions of Green’s functions. Thus, the KFBI method is said to be kernel-free. After solving an equivalent interface problem on a Cartesian grid by the FDM or the FEM, we quadratically interpolate the discrete solution at the discretization nodes of the domain boundary to evaluate the values of the boundary and volume integrals. We point out that the KFBI method can preserve the symmetric and positive definite property of the coefficient matrix of the discrete linear system of the equivalent interface problem. Hence, the discrete linear system can be efficiently solved with the standard geometric multigrid iterations or the fast Fourier transform based solvers. To show the numerical performance of the KFBI method, we simulate the bidomain equations on different complex regions such as the heart-shaped domain and a real human left ventricle (LV) space model in two- and three-dimensional spaces, respectively.

## 2 The Model

The bidomain equation which is governed by a singularly perturbed reaction-diffusion system consists of a set of nonlinear ordinary differential equations representing cell membrane dynamics and the partial differential equations representing the propagation of the electrical signal through the cardiac tissue [26]. Let  $\Omega \subset \mathbb{R}^d$  ( $d = 2$  or  $3$ ) be the bounded region occupied by the cardiac tissue which is usually complicated. We begin with the bidomain equation which consists of the equations for the intra- and extracellular potentials,  $\Phi_i$  and  $\Phi_e$ , coupled through the transmembrane potential  $V_m = \Phi_i - \Phi_e$ , for  $\mathbf{x} \in \Omega$  and  $t > 0$

$$\begin{aligned}
C_m \frac{\partial V_m}{\partial t} + I_{\text{ion}}(V_m, \mathbf{q}) &= \frac{1}{\beta} \nabla \cdot (\mathbf{D}_i \nabla \Phi_i), \\
C_m \frac{\partial V_m}{\partial t} + I_{\text{ion}}(V_m, \mathbf{q}) &= -\frac{1}{\beta} \nabla \cdot (\mathbf{D}_e \nabla \Phi_e) - I_{\text{stim}}, \\
\frac{\partial \mathbf{q}}{\partial t} &= \mathcal{M}(V_m, \mathbf{q}),
\end{aligned} \tag{1}$$

where  $C_m$  is the membrane capacitance per unit area;  $\beta$  is a surface to volume ratio of the cardiac cells;  $\mathbf{D}_i$  and  $\mathbf{D}_e$  are the space dependent intracellular and extracellular conductivity tensors, respectively;  $\mathbf{q}$  is a set of state variables;  $I_{\text{ion}}(V_m, \mathbf{q})$  and  $\mathcal{M}(V_m, \mathbf{q})$  are two known functions approximating the cellular membrane dynamics;  $I_{\text{stim}} = I_{\text{stim}}(t, \mathbf{x})$  is a given extracellular stimulus current. In this work, we consider the case that the cardiac tissue is insulated, *i.e.*, the bidomain equation subject to the homogeneous Neumann boundary condition

$$\mathbf{n} \cdot (\mathbf{D}_i \nabla \Phi_i) = 0 \quad \text{and} \quad \mathbf{n} \cdot (\mathbf{D}_e \nabla \Phi_e) = 0 \quad \text{on} \quad \partial\Omega, \tag{2}$$

where  $\mathbf{n}$  is the unit outward normal to the boundary  $\partial\Omega$  and imposed on  $\partial\Omega$  all the time. Provided some appropriate initial conditions on the intracellular potential  $\Phi_i$ , the extracellular potential  $\Phi_e$ , and the vector of the state variables  $\mathbf{q}$ , the bidomain equations can be numerically solved with some specific spatial discretization and temporal integration methods.

### 3 Operator Splitting Techniques

Operator splitting techniques [9, 10, 27] are widely used to efficiently solve the bidomain equations by decoupling the reaction and diffusion parts in the reaction-diffusion system to be solved. The application of an operator splitting technique allows integrating the reaction and diffusion parts independently and implicitly without solving a large nonlinear system in each time step. Let  $\Delta t > 0$  be the timestep and  $t^n = n\Delta t$  be the discrete times. The second-order Strang splitting is applied to numerically simulate the electrical activity of the cardiac tissue by integrating the decoupled parts in a symmetric way in the following three steps.

step 1: First half time step nonlinear reaction

$$\begin{aligned}
C_m \frac{\partial V_m}{\partial t} &= -I_{\text{ion}}(V_m, \mathbf{q}) \quad \text{for } t^n < t < t^n + \frac{\Delta t}{2}, \\
\frac{\partial \mathbf{q}}{\partial t} &= \mathcal{M}(V_m, \mathbf{q}) \quad \text{for } t^n < t < t^n + \frac{\Delta t}{2}.
\end{aligned} \tag{3}$$

step 2: A full time step linear diffusion

$$\begin{aligned}
C_m \frac{\partial V_m}{\partial t} &= \frac{1}{\beta} \nabla \cdot (\mathbf{D}_i \nabla \Phi_i) \quad \text{for } t^n < t < t^{n+1}, \\
C_m \frac{\partial V_m}{\partial t} &= -\frac{1}{\beta} \nabla \cdot (\mathbf{D}_e \nabla \Phi_e) - I_{\text{stim}} \quad \text{for } t^n < t < t^{n+1}.
\end{aligned} \tag{4}$$

step 3: Second half time step nonlinear reaction

$$\begin{aligned}
C_m \frac{\partial V_m}{\partial t} &= -I_{\text{ion}}(V_m, \mathbf{q}) \quad \text{for } t^n + \frac{\Delta t}{2} < t < t^{n+1}, \\
\frac{\partial \mathbf{q}}{\partial t} &= \mathcal{M}(V_m, \mathbf{q}) \quad \text{for } t^n + \frac{\Delta t}{2} < t < t^{n+1}.
\end{aligned} \tag{5}$$

Here, Eqs. (3) and (5) represent the resulting nonlinear reaction equations which are space independent and usually are stiff [28, 29] while Eq. (4) represents the resulting linear diffusion equation which is space

dependent. After the application of the Strang operator splitting, the reaction and diffusion equations can be separately discretized by implicit integration methods such as the backward Euler method, semi-implicit method, and the Crank-Nicolson to satisfy the stability requirement without solving a large nonlinear system [30]. To be specific, during each timestep, we integrate the reaction equations (3) and (5) by the forward Euler method and the backward Euler method, respectively, and integrate the diffusion equation (4) by the second-order implicit midpoint scheme.

For ease of illustration, we first give the implicit midpoint scheme for the abstract form

$$\frac{du(t)}{dt} = f(u), \text{ for } t > 0, \quad (6)$$

which can then be straightforwardly extended to the bidomain equations. The implicit midpoint scheme for Eq. (6) is given by

$$\frac{u^{n+1} - u^n}{\Delta t} = f\left(\frac{u^{n+1} + u^n}{2}\right),$$

and can be rewritten as the discrete format obtained from the application of the backward Euler method

$$\frac{w - u^n}{\Delta t/2} = f(w),$$

where  $w = (u^{n+1} + u^n)/2$  and the corresponding timestep is  $\Delta t/2$ . In our implementation, we first obtain the numerical solution of the intermediate variable  $w$  and then compute the numerical solution  $u^{n+1} = 2w - u^n$ . Therefore, we restrict ourselves to the discussion on the application of the backward Euler method to integrate the diffusion equation (4). Time integration of the diffusion equation by the backward Euler method from time  $t^n$  to time  $t^{n+1}$  leads to the semi-discrete partial differential equations

$$\begin{aligned} C_m \frac{V_m^{n+1} - V_m^n}{\Delta t} &= \frac{1}{\beta} \nabla \cdot (\mathbf{D}_i \nabla \Phi_i^{n+1}), \\ C_m \frac{V_m^{n+1} - V_m^n}{\Delta t} &= -\frac{1}{\beta} \nabla \cdot (\mathbf{D}_e \nabla \Phi_e^{n+1}) - I_{\text{stim}}, \end{aligned} \quad (7)$$

where  $V_m^n$ ,  $\Phi_i^n$ , and  $\Phi_e^n$  are the finite difference approximations of the variables  $V_m$ ,  $\Phi_i$ , and  $\Phi_e$  at time  $t^n$ , respectively.

Assume that the extracellular stimulus current is only space dependent. We rewrite the semi-discrete partial differential equations (7) as

$$\begin{aligned} \nabla \cdot (\mathbf{D}_i \nabla \Phi_i^{n+1}) - \kappa(\Phi_i^{n+1} - \Phi_e^{n+1}) &= -\kappa V_m^n, \\ \nabla \cdot (\mathbf{D}_e \nabla \Phi_e^{n+1}) + \kappa(\Phi_i^{n+1} - \Phi_e^{n+1}) &= \kappa V_m^n - \beta I_{\text{stim}}, \end{aligned} \quad (8)$$

where  $\kappa = C_m \beta / \Delta t$ . Denote the unknown vector function and the right hand side of the system (8) by  $\mathbf{u} \equiv (\Phi_i^{n+1}, \Phi_e^{n+1})^T$  and  $\mathbf{f} \equiv (-\kappa V_m^n, \kappa V_m^n - \beta I_{\text{stim}})^T$ . Define Eq. (8) in the form of modified Helmholtz equation as followed

$$(\mathcal{L}\mathbf{u}) \equiv \nabla \cdot (\mathbf{D}\nabla\mathbf{u}) - \mathbf{K}\mathbf{u} = \mathbf{f} \quad \text{in } \Omega, \quad (9)$$

where  $\mathbf{D} \equiv \begin{pmatrix} \mathbf{D}_i & 0 \\ 0 & \mathbf{D}_e \end{pmatrix}$  and  $\mathbf{K} \equiv \begin{pmatrix} \kappa & -\kappa \\ -\kappa & \kappa \end{pmatrix}$ . The corresponding boundary condition is homogeneous Neumann boundary condition which is noted as

$$\mathbf{g}^N \equiv \mathbf{n} \cdot (\mathbf{D}\nabla\mathbf{u}) \equiv (\mathbf{n} \cdot (\mathbf{D}_i \nabla \Phi_i), \mathbf{n} \cdot (\mathbf{D}_e \nabla \Phi_e))^T = \mathbf{0}. \quad (10)$$

In the following sections 4 and 5, we introduce how to solve the boundary value problem (9) by the KFBI method during each timestep.

## 4 Boundary Integral Equation Formulation

In this section, we reformulate the homogeneous Neumann boundary value problem (9) as a BIE [23]. Let  $\mathcal{B}$  be a larger regular domain which completely contains the computational domain  $\Omega$  and  $\partial\Omega$  be the smooth interface in  $\mathcal{B}$  which separates the larger regular domain  $\mathcal{B}$  into two subdomains  $\Omega$  and  $\Omega^C$ . Let  $G(\mathbf{q}; \mathbf{p})$  be Green's function associated with the operator defined in Eq. (9) on the larger regular domain  $\mathcal{B}$ , which satisfies

$$\begin{aligned} \mathcal{L}G(\mathbf{q}; \mathbf{p}) &\equiv \nabla_{\mathbf{q}} \cdot (\mathbf{D}\nabla_{\mathbf{q}}G) - \mathbf{K}G = \delta(\mathbf{q} - \mathbf{p}) \quad \mathbf{q} \in \mathcal{B}, \\ \mathbf{n}_{\mathbf{q}} \cdot (\mathbf{D}\nabla_{\mathbf{q}}G(\mathbf{q}; \mathbf{p})) &= 0 \quad \mathbf{q} \in \partial\mathcal{B}, \end{aligned} \quad (11)$$

for each fixed  $\mathbf{p} \in \mathcal{B}$ . Here,  $\delta(\mathbf{q} - \mathbf{p})$  is the Dirac delta function;  $\nabla_{\mathbf{q}}$  stands for the gradient operator with respect to the space variable  $\mathbf{q} \in \mathbb{R}^d$ . In terms of the Green's function  $G(\mathbf{q}; \mathbf{p})$ , the solution to the Neumann boundary value problem defined by Eqs. (9) and (10) can be expressed as a sum of a volume integral and a boundary integral

$$\mathbf{u}(\mathbf{p}) = \int_{\Omega} G(\mathbf{q}; \mathbf{p})\mathbf{f}(\mathbf{q})d\mathbf{q} - \int_{\partial\Omega} G(\mathbf{q}; \mathbf{p})\psi(\mathbf{q})ds_{\mathbf{q}}, \quad \mathbf{p} \in \Omega, \quad (12)$$

where the density  $\psi(\mathbf{p})$  satisfies the second kind Fredholm BIE

$$\frac{1}{2}\psi(\mathbf{p}) - \int_{\partial\Omega} \mathbf{n}_{\mathbf{p}} \cdot \mathbf{D}\nabla_{\mathbf{p}}G(\mathbf{q}; \mathbf{p})\psi(\mathbf{q})ds_{\mathbf{q}} = \mathbf{g}^N - \mathbf{n}_{\mathbf{p}} \cdot \mathbf{D}\nabla_{\mathbf{p}} \left( \int_{\Omega} G(\mathbf{q}; \mathbf{p})\mathbf{f}(\mathbf{q})d\mathbf{q} \right), \quad \mathbf{p} \in \partial\Omega. \quad (13)$$

We can solve the BIE (13) by the following simple iterations

$$\begin{aligned} \psi_{\nu+1}(\mathbf{p}) &= \psi_{\nu}(\mathbf{p}) + 2\gamma \left[ \mathbf{g}^N - \mathbf{n}_{\mathbf{p}} \cdot \mathbf{D}\nabla_{\mathbf{p}} \left( \int_{\Omega} G(\mathbf{q}; \mathbf{p})\mathbf{f}(\mathbf{q})d\mathbf{q} \right) \right. \\ &\quad \left. - \left( \frac{1}{2}\psi_{\nu}(\mathbf{p}) - \int_{\partial\Omega} \mathbf{n}_{\mathbf{p}} \cdot \mathbf{D}\nabla_{\mathbf{p}}G(\mathbf{q}; \mathbf{p})\psi_{\nu}(\mathbf{q})ds_{\mathbf{q}} \right) \right], \quad \mathbf{p} \in \partial\Omega \end{aligned} \quad (14)$$

for  $\nu = 0, 1, 2, \dots$ , with an iteration parameter  $\gamma \in (0, 1)$ . Giving a prescribed tolerance and any initial guess of the density, we can get a numerical approximation to the unknown density function  $\psi$  once the simple iteration converges. However, it is difficult to calculate the boundary integral and volume integral in Eqs. (13) and (14) using the general numerical integration methods since the analytic expressions of Green's functions, *i.e.*, the kernels of the integrals are unavailable. Hence, the KFBI method is a new strategy to evaluate the integrals approximately without using the analytical expressions of Green's functions which will be described in the next section. The BIE (13) can be further noted as  $\mathcal{A}\psi = \mathbf{g}$  where  $\mathcal{A}\psi \equiv \frac{1}{2}\psi(\mathbf{p}) - \int_{\partial\Omega} \mathbf{D}\mathbf{n}_{\mathbf{p}} \cdot \nabla_{\mathbf{p}}G(\mathbf{q}; \mathbf{p})\psi(\mathbf{q})ds_{\mathbf{q}}$  and  $\mathbf{g} \equiv \mathbf{g}^N - \mathbf{n}_{\mathbf{p}} \cdot \mathbf{D}\nabla_{\mathbf{p}} \left( \int_{\Omega} G(\mathbf{q}; \mathbf{p})\mathbf{f}(\mathbf{q})d\mathbf{q} \right)$ . The simple iterations for solving the BIE  $\mathcal{A}\psi = \mathbf{g}$  could be further improved by a Krylov subspace method such as the GMRES iteration [25, 31].

## 5 The Kernel-Free Boundary Integral Method

Once again, the KFBI method is used to approximately evaluate the volume and boundary integrals arising from the right hand side  $\mathbf{g}$  of the BIE  $\mathcal{A}\psi = \mathbf{g}$  and the matrix-vector multiplication  $\mathcal{A}\psi$  during the Krylov subspace iteration [31]. The KFBI method first replaces the evaluation of the integrals by the solutions of the equivalent simple interface problems on the larger regular domain  $\mathcal{B}$  without calling for computing any approximation of Green's functions. After discretizing the simple interface problem by the FDM on a Cartesian grid of the larger regular domain  $\mathcal{B}$ , the obtained discrete system can be solved efficiently by a fast Fourier transform (FFT) based solver after applying an appropriate correction

to the right hand side of the discrete system at the irregular grid nodes. Noticing that the boundary and volume integrals in Eqs. (13) and (14) are restricted at the discretization nodes of the interface  $\partial\Omega$ , we approximate the limiting values of the integrals by taking polynomial interpolation of the discrete numerical solutions.

## 5.1 Reinterpret the integrals

Assume that all of the variables and functions encountered are smooth enough such that the derivatives that appear are meaningful. A piecewise smooth dependent variable  $\omega(\mathbf{p})$  which is defined on the larger regular domain  $\mathcal{B}$  have possible discontinuities only on the domain boundary  $\partial\Omega$ . let  $\omega^+(\mathbf{p})$  and  $\omega^-(\mathbf{p})$  be the restrictions of  $\omega(\mathbf{p})$  on the subdomains  $\Omega$  and  $\Omega^C$ , respectively. For  $\mathbf{p} \in \partial\Omega$ , let

$$\omega^+(\mathbf{p}) \equiv \lim_{\substack{\mathbf{q} \in \Omega \\ \mathbf{q} \rightarrow \mathbf{p}}} \omega(\mathbf{q}) \quad \text{and} \quad \omega^-(\mathbf{p}) \equiv \lim_{\substack{\mathbf{q} \in \Omega^C \\ \mathbf{q} \rightarrow \mathbf{p}}} \omega(\mathbf{q}) \quad (15)$$

be the limit values of  $\omega(\mathbf{p})$  from either side of the domain boundary. The jump of the variable  $\omega(\mathbf{p})$  across the interface is denoted by

$$[\omega(\mathbf{p})] \equiv \omega^+(\mathbf{p}) - \omega^-(\mathbf{p}) \quad (16)$$

with  $\mathbf{p} \in \partial\Omega$ . The jumps of a vector functions across the interface can be defined in the same way.

The volume integral  $\mathbf{v}(\mathbf{p}) = (\mathcal{G}\mathbf{f})(\mathbf{p}) \equiv \int_{\Omega} G(\mathbf{q}; \mathbf{p})\mathbf{f}(\mathbf{q})d\mathbf{q}$  satisfies the interface problem

$$\begin{aligned} \nabla \cdot (\mathbf{D}\nabla\mathbf{v}) - \mathbf{K}\mathbf{v} &= \tilde{\mathbf{f}} && \text{in } \mathcal{B} \setminus \partial\Omega, \\ [\mathbf{v}] &= 0 && \text{on } \partial\Omega, \\ \mathbf{n} \cdot [\mathbf{D}\nabla\mathbf{v}] &= 0 && \text{on } \partial\Omega, \\ \mathbf{v} &= 0 && \text{on } \partial\mathcal{B}. \end{aligned} \quad (17)$$

The equivalent interface problem of the volume integral is a partial differential equation with Dirichlet boundary condition which can be solved easily. Here, the source function in Eq.(9)  $\mathbf{f} = (-\kappa V_m^n, \kappa V_m^n - \beta I_{\text{stim}})^T$  is a vector function without analytical expression consisting of the discrete solution of the transmembrane voltage at the last discrete time. If we set the  $\tilde{\mathbf{f}}$  is zero in the subdomain  $\Omega^C$  and equal to  $\mathbf{f}$  in the subdomain  $\Omega$ , it is not easy to compute the jump of  $\tilde{\mathbf{f}}$  at the discretization nodes of the domain boundary during solving the equivalent interface problems. According to the continuous properties of the volume integral and the boundary integral [23, 32], we continuously extend the vector function  $\mathbf{f}(\mathbf{p})$  ( $\mathbf{p} \in \Omega$ ) by evaluating the transmembrane voltage  $V_m$  in the larger regular domain  $\mathcal{B}$  at the very beginning and approximately estimate the value of  $\mathbf{n}_p \cdot \mathbf{D}\nabla_p (\int_{\Omega} G(\mathbf{q}; \mathbf{p})\mathbf{f}(\mathbf{q})d\mathbf{q})$  by taking polynomial interpolation of the discrete numerical solution of the equivalent interface problem, *i.e.*, the value of  $\mathbf{g}$  in the BIE  $\mathcal{A}\psi = \mathbf{g}$ .

The boundary integral  $\mathbf{v}(\mathbf{p}) = -(\mathcal{K}\psi)(\mathbf{p}) \equiv -\int_{\partial\Omega} G(\mathbf{q}; \mathbf{p})\psi(\mathbf{q})ds_{\mathbf{q}}$  satisfies the interface problem

$$\begin{aligned} \nabla \cdot (\mathbf{D}\nabla\mathbf{v}) - \mathbf{K}\mathbf{v} &= 0 && \text{in } \mathcal{B} \setminus \partial\Omega, \\ [\mathbf{v}] &= 0 && \text{on } \partial\Omega, \\ \mathbf{n} \cdot [\mathbf{D}\nabla\mathbf{v}] &= \psi && \text{on } \partial\Omega, \\ \mathbf{v} &= 0 && \text{on } \partial\mathcal{B}. \end{aligned} \quad (18)$$

The boundary integral is continuous across the interface  $\partial\Omega$  while the normal flux of the boundary integral  $\mathbf{n}_p \cdot [\mathbf{D}\nabla_p\mathbf{v}]$  has a jump [23] with strength equal to  $\psi(\mathbf{p})$ , *i.e.*,

$$\mathbf{v}^+(\mathbf{p}) = \mathbf{v}^-(\mathbf{p}) \quad \text{on } \partial\Omega \quad (19)$$

and

$$\mathbf{n} \cdot (\mathbf{D}\nabla\mathbf{v}^+)(\mathbf{p}) - \mathbf{n} \cdot (\mathbf{D}\nabla\mathbf{v})(\mathbf{p}) = \frac{1}{2}\psi(\mathbf{p}) \quad \text{on } \partial\Omega \quad (20)$$

$$\mathbf{n} \cdot (\mathbf{D}\nabla\mathbf{v}^-)(\mathbf{p}) - \mathbf{n} \cdot (\mathbf{D}\nabla\mathbf{v})(\mathbf{p}) = -\frac{1}{2}\psi(\mathbf{p}) \quad \text{on } \partial\Omega \quad (21)$$

For the interior boundary value problems, the discontinuity property of the boundary integral presented in Eq.(20) is used to evaluate the left hand side of the BIE (13), *i.e.*, the matrix-vector multiplication  $\mathcal{A}\psi$ . Moreover, the solutions of the above interface problems are both continuous across the interface which makes the extension of the  $\mathbf{f}$  to  $\tilde{\mathbf{f}}$  be reasonable. We point out that the above two interface problems defined in Eqs. (17) and (18) can be presented and solved in a unified framework.

## 5.2 Discretization of the PDE on a Cartesian grid

We discretize the partial differential equation

$$\mathcal{L}\mathbf{u}(\mathbf{p}) \equiv \nabla \cdot (\mathbf{D}\nabla\mathbf{u}) - \mathbf{K}\mathbf{u} = \mathbf{f}(\mathbf{p}), \quad \mathbf{p} \in \mathcal{B} \setminus \partial\Omega \quad (22)$$

on a Cartesian grid of the larger regular domain  $\mathcal{B}$  with the FDM. In this work, we only present the finite difference discretization scheme in two-dimensional space since the finite difference discretization scheme in three-dimensional space is similar to that in two-dimensional space. For simplicity, we assume that the larger regular domain  $\mathcal{B} = (a, b) \times (c, d)$  is a square which is partitioned into a uniform  $I \times I$  Cartesian grid with the mesh parameter  $h = (b - a)/I$ . Let  $x_k = a + kh$  and  $y_l = c + lh$  for  $k = 0, 1, \dots, I$  and  $l = 0, 1, \dots, I$ . Denote the  $(k, l)$ -th node of the Cartesian grid by  $\mathbf{p}_{k,l} = (x_k, y_l)^T$ . Omitting the superscripts representing the discrete times, we denote the finite difference approximation of the solution  $\mathbf{u}$  at the  $(k, l)$ -th grid node  $\mathbf{p}_{k,l}$  by  $\mathbf{u}_{k,l} = (\Phi_{k,l}^i, \Phi_{k,l}^e)^T$ . For the bidomain simulations, we model the square as consisting of fibers that lie parallel to the  $x$ -axis, *i.e.*, the conductivity tensors  $\mathbf{D}_i$  and  $\mathbf{D}_e$  are diagonal matrices. Denote the intra- and extracellular conductivity tensors by  $\mathbf{D}_i = \text{diag}(\sigma_i, \eta_i)$  and  $\mathbf{D}_e = \text{diag}(\sigma_e, \eta_e)$  and denote the source function by  $\mathbf{f} = (f^i, f^e)^T$ . With the second-order centered finite difference method, the PDE (22) is discretized into the finite difference equations

$$\begin{aligned} \frac{s_{k,l} - 2\sigma_i\Phi_{k,l}^i - 2\eta_i\Phi_{k,l}^i}{h^2} - \kappa\Phi_{k,l}^i + \kappa\Phi_{k,l}^e &= f_{k,l}^i, \\ \frac{t_{k,l} - 2\sigma_e\Phi_{k,l}^e - 2\eta_e\Phi_{k,l}^e}{h^2} + \kappa\Phi_{k,l}^i - \kappa\Phi_{k,l}^e &= f_{k,l}^e, \end{aligned} \quad (23)$$

where

$$s_{k,l} = \sigma_i(\Phi_{k+1,l}^i + \Phi_{k-1,l}^i) + \eta_i(\Phi_{k,l+1}^i + \Phi_{k,l-1}^i), \quad (24)$$

$$t_{k,l} = \sigma_e(\Phi_{k+1,l}^e + \Phi_{k-1,l}^e) + \eta_e(\Phi_{k,l+1}^e + \Phi_{k,l-1}^e), \quad (25)$$

for  $k = 0, 1, \dots, I$  and  $l = 0, 1, \dots, I$ . In two- and three-dimensional spaces, the finite difference equation at each Cartesian grid node  $\mathbf{p}_{k,l}$  involves a five-point stencil and a seven-point stencil, respectively. When the coefficients  $\sigma_i, \sigma_e, \eta_i, \eta_e, \kappa$ , and the source function  $\mathbf{f}$  are sufficiently smooth, the solution to the finite difference equation (23) has a second-order accuracy, irrespective of the interface  $\partial\Omega$ .

## 5.3 Correction of the discrete system

Owing to the existence of the interface  $\partial\Omega$ , the Cartesian grid nodes  $\mathbf{p}_{k,l}$  are divided into regular nodes and irregular nodes. A grid node is called irregular if its finite difference stencil has intersections with the domain boundary  $\partial\Omega$ . Otherwise, the grid nodes are called regular. The local truncation errors of the

finite difference equations (23) at irregular grid nodes are much larger than those at regular grid nodes. Specifically, the estimate for the local truncation errors at irregular grid nodes is  $\mathcal{O}(h^{-2})$  with mesh parameter  $h$  [24]. Because of the large local truncation errors at irregular grid nodes, the solution to the discrete system obtained from the equivalent interface problem is inaccurate. Hence, we need to correct the finite difference equations at irregular grid nodes to get an accurate solution.

Denote the smooth solution in subdomains  $\Omega$  and  $\Omega^C$  by  $\mathbf{u}^+$  and  $\mathbf{u}^-$ . In the case of two-dimensional space, we assume that the five-point stencil of an irregular grid node  $\mathbf{p}_{k,l}$  intersects the domain boundary  $\partial\Omega$  only once and the intersection point located at the horizontal grid line is  $(z_k, y_l)$  with  $x_k \leq z_k < x_{k+1}$ . In the next, we estimate the local truncation error at the irregular grid node  $\mathbf{p}_{k,l}$

$$E_{h,x}^i(x_k, y_l) \equiv \frac{\sigma_i ((\Phi^i)^-(x_{k+1}, y_l) + (\Phi^i)^+(x_{k-1}, y_l) - 2(\Phi^i)^+(x_k, y_l))}{h^2} - \sigma_i \frac{\partial^2}{\partial x^2} (\Phi^i)^+(x_k, y_l), \quad (26)$$

$$E_{h,x}^e(x_k, y_l) \equiv \frac{\sigma_e ((\Phi^e)^-(x_{k+1}, y_l) + (\Phi^e)^+(x_{k-1}, y_l) - 2(\Phi^e)^+(x_k, y_l))}{h^2} - \sigma_e \frac{\partial^2}{\partial x^2} (\Phi^e)^+(x_k, y_l). \quad (27)$$

We first make Taylor expansions for  $(\Phi^i)^+(x_{k+1}, y_l)$ ,  $(\Phi^e)^+(x_{k+1}, y_l)$ ,  $(\Phi^i)^-(x_{k+1}, y_l)$ , and  $(\Phi^e)^-(x_{k+1}, y_l)$  around the intersection point  $(z_k, y_l)$ ,

$$\begin{aligned} (\Phi^i)^\pm(x_{k+1}, y_l) &= (\Phi^i)^\pm(z_k, y_l) + \partial_x (\Phi^i)^\pm(z_k, y_l)(x_{k+1} - z_k) + \frac{1}{2} \partial_{xx} (\Phi^i)^\pm(z_k, y_l)(x_{k+1} - z_k)^2 \\ &\quad + \frac{1}{6} \partial_{xxx} (\Phi^i)^\pm(z_k, y_l)(x_{k+1} - z_k)^3 + O(h^4), \end{aligned}$$

and

$$\begin{aligned} (\Phi^e)^\pm(x_{k+1}, y_l) &= (\Phi^e)^\pm(z_k, y_l) + \partial_x (\Phi^e)^\pm(z_k, y_l)(x_{k+1} - z_k) + \frac{1}{2} \partial_{xx} (\Phi^e)^\pm(z_k, y_l)(x_{k+1} - z_k)^2 \\ &\quad + \frac{1}{6} \partial_{xxx} (\Phi^e)^\pm(z_k, y_l)(x_{k+1} - z_k)^3 + O(h^4). \end{aligned}$$

We then estimate the leading order term of the local truncation error  $E_{h,x}^i(x_k, y_l)$  and  $E_{h,x}^e(x_k, y_l)$  as

$$\begin{aligned} \frac{(\Phi^i)^+(x_{k+1}, y_l) - (\Phi^i)^-(x_{k+1}, y_l)}{h^2} &= \frac{1}{h^2} \left\{ [\Phi^i] + [\partial_x \Phi^i](x_{k+1} - z_k) + \frac{1}{2} [\partial_{xx} \Phi^i](x_{k+1} - z_k)^2 \right. \\ &\quad \left. + \frac{1}{6} [\partial_{xxx} \Phi^i](x_{k+1} - z_k)^3 \right\} + O(h^2) \end{aligned}$$

and

$$\begin{aligned} \frac{(\Phi^e)^+(x_{k+1}, y_l) - (\Phi^e)^-(x_{k+1}, y_l)}{h^2} &= \frac{1}{h^2} \left\{ [\Phi^e] + [\partial_x \Phi^e](x_{k+1} - z_k) + \frac{1}{2} [\partial_{xx} \Phi^e](x_{k+1} - z_k)^2 \right. \\ &\quad \left. + \frac{1}{6} [\partial_{xxx} \Phi^e](x_{k+1} - z_k)^3 \right\} + O(h^2). \end{aligned}$$

Here,  $[\Phi^i] = (\Phi^i)^+(z_k, y_l) - (\Phi^i)^-(z_k, y_l)$ ,  $[\Phi^e] = (\Phi^e)^+(z_k, y_l) - (\Phi^e)^-(z_k, y_l)$ ,  $[\partial_x \Phi^i] = \partial_x (\Phi^i)^+(z_k, y_l) - \partial_x (\Phi^i)^-(z_k, y_l)$ ,  $[\partial_x \Phi^e] = \partial_x (\Phi^e)^+(z_k, y_l) - \partial_x (\Phi^e)^-(z_k, y_l)$ ,  $[\partial_{xx} \Phi^i] \equiv \partial_{xx} (\Phi^i)^+(z_k, y_l) - \partial_{xx} (\Phi^i)^-(z_k, y_l)$ ,



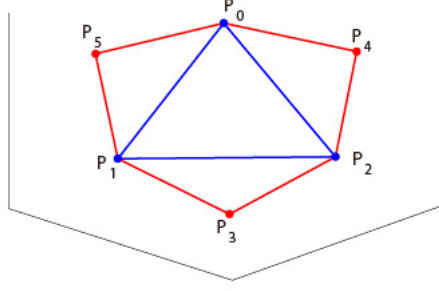


Figure 1: Six boundary points of a local coordinate system.

and  $[\partial_{xx}\Phi^e] \equiv \partial_{xx}(\Phi^e)^+(z_k, y_l) - \partial_{xx}(\Phi^e)^-(z_k, y_l)$  are the jumps of the function and its partial derivatives across the interface.

The correction of the discrete system at the irregular grid node  $\mathbf{p}_{k,l}$  is given by the following quantity

$$(C_{h,x}^i)^+ = \frac{\sigma_i}{h^2} \left( [\Phi^i] + [\partial_x \Phi^i](x_{k+1} - z_k) + \frac{1}{2} [\partial_{xx} \Phi^i](x_{k+1} - z_k)^2 \right) \quad (28)$$

$$(C_{h,x}^e)^+ = \frac{\sigma_e}{h^2} \left( [\Phi^e] + [\partial_x \Phi^e](x_{k+1} - z_k) + \frac{1}{2} [\partial_{xx} \Phi^e](x_{k+1} - z_k)^2 \right) \quad (29)$$

The jumps of the function and its partial derivatives across the interface are derived from the interface conditions of the equivalent interface problem [23, 24]. In three-dimensional space, we calculate the corresponding jumps by constructing local coordinate systems on the discrete triangle grid which represents the domain boundary  $\partial\Omega$ . As shown in Fig. 1, the local coordinate system of a triangle element consists of the six boundary points around it.

When the interface intersects the finite difference stencil multiple times, we should calculate all the corresponding terms  $(C_{h,x}^i)^\pm$ ,  $(C_{h,x}^e)^\pm$ ,  $(C_{h,y}^i)^\pm$ ,  $(C_{h,y}^e)^\pm$ ,  $(C_{h,z}^i)^\pm$ , and  $(C_{h,z}^e)^\pm$  to modify the right hand side of the discrete linear system (22). In general, for an irregular grid node  $(x_k, y_l)$  in two-dimensional space, the finite difference equation turns to

$$\begin{aligned} \frac{s_{k,l} - 2\sigma_i \Phi_{k,l}^i - 2\eta_i \Phi_{k,l}^i}{h^2} - \kappa \Phi_{k,l}^i + \kappa \Phi_{k,l}^e &= f_{k,l}^i + C_h^i, \\ \frac{t_{k,l}}{h^2 - 2\sigma_e \Phi_{k,l}^e - 2\eta_e \Phi_{k,l}^e} + \kappa \Phi_{k,l}^i - \kappa \Phi_{k,l}^e &= f_{k,l}^e + C_h^e. \end{aligned} \quad (30)$$

where  $C_h^i$  and  $C_h^e$  are the sum of all corrections at the irregular grid node  $(x_k, y_l)$  of the variable  $\Phi^i$  and  $\Phi^e$ , respectively. After appropriately modifying the right hand side of the discrete linear system, the local truncation error of the obtained discrete linear system is of first-order at irregular grid nodes and its solution has essentially second-order accuracy [23, 33]. Since the modification at irregular grid nodes does not change the symmetric and positive definite coefficient matrix, the discrete linear system of the equivalent interface problem can be solved efficiently by an FFT based Poisson solver [34, 35].

#### 5.4 Interpolation of the volume and boundary integrals

Denote  $\mathbf{u}_{\nu,h}(\mathbf{p}) = (\Phi_{\nu,h}^i, \Phi_{\nu,h}^e)^T$  as the solution of the discrete linear system obtained after appropriate correction at the irregular grid nodes and  $\nu$  is the iteration number of the iteration method for solving the

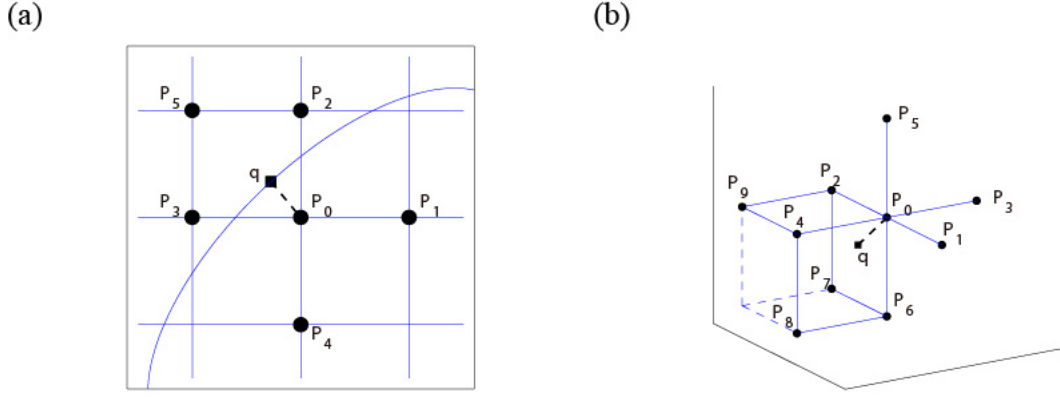


Figure 2: Illustration of a six-point and a ten-point interpolation stencil of the discretization node  $\mathbf{q}$  of the boundary curve.

BIE (13). We make Taylor expansions for the approximate solution  $\mathbf{u}_{\nu,h}$  is to extract the limit values of  $\mathbf{n} \cdot (\mathbf{D}\nabla \mathbf{u}_{\nu,h}^+)$ , *i.e.*, the values of  $\partial_x \Phi_i^+$ ,  $\partial_x \Phi_e^+$ ,  $\partial_y \Phi_i^+$ ,  $\partial_y \Phi_e^+$ ,  $\partial_z \Phi_i^+$ , and  $\partial_z \Phi_e^+$  at the discretization nodes of the boundary curve  $\partial\Omega$ . As shown in Fig. 2, a six-point interpolation stencil in two-dimensional space or a ten-point interpolation stencil in three-dimensional space is required to evaluate the limit values at a discretization node  $\mathbf{q}$  of the boundary curve by quadratic interpolation.

For a Cartesian grid node  $\mathbf{p} \in \Omega \subset \mathbb{R}^2$ , the Taylor expansion for the approximate solution  $\mathbf{u}_{\nu,h}(\mathbf{p}) = (\Phi_{\nu,h}^i(\mathbf{p}), \Phi_{\nu,h}^e(\mathbf{p}))^T$  around the discretization node  $\mathbf{q}$  of the boundary curve is as followed

$$\begin{aligned} \Phi_{\nu,h}^i(\mathbf{p}) &= (\Phi_{\nu,h}^i)^+(\mathbf{q}) + \frac{\partial(\Phi_{\nu,h}^i)^+(\mathbf{q})}{\partial x} \xi + \frac{\partial(\Phi_{\nu,h}^i)^+(\mathbf{q})}{\partial y} \eta \\ &+ \frac{1}{2} \frac{\partial^2(\Phi_{\nu,h}^i)^+(\mathbf{q})}{\partial x^2} \xi^2 + \frac{\partial^2(\Phi_{\nu,h}^i)^+(\mathbf{q})}{\partial x \partial y} \xi \eta + \frac{1}{2} \frac{\partial^2(\Phi_{\nu,h}^i)^+(\mathbf{q})}{\partial y^2} \eta^2 + O(|\mathbf{p} - \mathbf{q}|^3), \end{aligned} \quad (31)$$

$$\begin{aligned} \Phi_{\nu,h}^e(\mathbf{p}) &= (\Phi_{\nu,h}^e)^+(\mathbf{q}) + \frac{\partial(\Phi_{\nu,h}^e)^+(\mathbf{q})}{\partial x} \xi + \frac{\partial(\Phi_{\nu,h}^e)^+(\mathbf{q})}{\partial y} \eta \\ &+ \frac{1}{2} \frac{\partial^2(\Phi_{\nu,h}^e)^+(\mathbf{q})}{\partial x^2} \xi^2 + \frac{\partial^2(\Phi_{\nu,h}^e)^+(\mathbf{q})}{\partial x \partial y} \xi \eta + \frac{1}{2} \frac{\partial^2(\Phi_{\nu,h}^e)^+(\mathbf{q})}{\partial y^2} \eta^2 + O(|\mathbf{p} - \mathbf{q}|^3). \end{aligned} \quad (32)$$

For a Cartesian grid node  $\mathbf{p} \in \Omega^C \subset \mathbb{R}^2$ , the Taylor expansion of the approximate solution  $\mathbf{u}_{\nu,h}(\mathbf{p}) = (\Phi_{\nu,h}^i(\mathbf{p}), \Phi_{\nu,h}^e(\mathbf{p}))^T$  around the discretization node  $\mathbf{q}$  of the boundary curve is as followed

$$\begin{aligned} \Phi_{\nu,h}^i(\mathbf{p}) &= (\Phi_{\nu,h}^i)^-(\mathbf{q}) + \frac{\partial(\Phi_{\nu,h}^i)^-(\mathbf{q})}{\partial x} \xi + \frac{\partial(\Phi_{\nu,h}^i)^-(\mathbf{q})}{\partial y} \eta \\ &+ \frac{1}{2} \frac{\partial^2(\Phi_{\nu,h}^i)^-(\mathbf{q})}{\partial x^2} \xi^2 + \frac{\partial^2(\Phi_{\nu,h}^i)^-(\mathbf{q})}{\partial x \partial y} \xi \eta + \frac{1}{2} \frac{\partial^2(\Phi_{\nu,h}^i)^-(\mathbf{q})}{\partial y^2} \eta^2 + O(|\mathbf{p} - \mathbf{q}|^3), \end{aligned} \quad (33)$$

$$\begin{aligned} \Phi_{\nu,h}^e(\mathbf{p}) &= (\Phi_{\nu,h}^e)^-(\mathbf{q}) + \frac{\partial(\Phi_{\nu,h}^e)^-(\mathbf{q})}{\partial x} \xi + \frac{\partial(\Phi_{\nu,h}^e)^-(\mathbf{q})}{\partial y} \eta \\ &+ \frac{1}{2} \frac{\partial^2(\Phi_{\nu,h}^e)^-(\mathbf{q})}{\partial x^2} \xi^2 + \frac{\partial^2(\Phi_{\nu,h}^e)^-(\mathbf{q})}{\partial x \partial y} \xi \eta + \frac{1}{2} \frac{\partial^2(\Phi_{\nu,h}^e)^-(\mathbf{q})}{\partial y^2} \eta^2 + O(|\mathbf{p} - \mathbf{q}|^3). \end{aligned} \quad (34)$$

Here,  $(\xi, \eta)^T \equiv \mathbf{p} - \mathbf{q}$ . Omit some subscripts by

$$\begin{aligned} V^\pm &\equiv (\Phi_{\nu,h}^i)^\pm(\mathbf{q}), & V_x^\pm &\equiv \frac{\partial(\Phi_{\nu,h}^i)^\pm(\mathbf{q})}{\partial x}, & V_y^\pm &\equiv \frac{\partial(\Phi_{\nu,h}^i)^\pm(\mathbf{q})}{\partial y}, \\ V_{xx}^\pm &\equiv \frac{\partial^2(\Phi_{\nu,h}^i)^\pm(\mathbf{q})}{\partial x^2}, & V_{xy}^\pm &\equiv \frac{\partial^2(\Phi_{\nu,h}^i)^\pm(\mathbf{q})}{\partial x \partial y}, & V_{yy}^\pm &\equiv \frac{\partial^2(\Phi_{\nu,h}^i)^\pm(\mathbf{q})}{\partial y^2}, \end{aligned} \quad (35)$$

and

$$\begin{aligned} W^\pm &\equiv (\Phi_{\nu,h}^e)^\pm(\mathbf{q}), & W_x^\pm &\equiv \frac{\partial(\Phi_{\nu,h}^e)^\pm(\mathbf{q})}{\partial x}, & W_y^\pm &\equiv \frac{\partial(\Phi_{\nu,h}^e)^\pm(\mathbf{q})}{\partial y}, \\ W_{xx}^\pm &\equiv \frac{\partial^2(\Phi_{\nu,h}^e)^\pm(\mathbf{q})}{\partial x^2}, & W_{xy}^\pm &\equiv \frac{\partial^2(\Phi_{\nu,h}^e)^\pm(\mathbf{q})}{\partial x \partial y}, & W_{yy}^\pm &\equiv \frac{\partial^2(\Phi_{\nu,h}^e)^\pm(\mathbf{q})}{\partial y^2}. \end{aligned} \quad (36)$$

Denote the six nearby grid nodes by  $\mathbf{p}_j$  ( $j = 0, 1, \dots, 5$ ). First, we evaluate the truncated Taylor series of  $\Phi_{\nu,h}^i$  which yield

$$V^+ + V_x^+ \xi_j + V_y^+ \eta_j + \frac{1}{2} V_{xx}^+ \xi_j^2 + V_{xy}^+ \xi_j \eta_j + \frac{1}{2} V_{yy}^+ \eta_j^2 = V_j \quad \text{if } \mathbf{P}_j \in \Omega \quad (37)$$

and

$$V^- + V_x^- \xi_j + V_y^- \eta_j + \frac{1}{2} V_{xx}^- \xi_j^2 + V_{xy}^- \xi_j \eta_j + \frac{1}{2} V_{yy}^- \eta_j^2 = V_j \quad \text{if } \mathbf{P}_j \in \Omega^C, \quad (38)$$

where  $V_j \equiv (\Phi_{\nu,h}^i)(\mathbf{p}_j)$  and  $(\xi_j, \eta_j)^T \equiv (\mathbf{p}_j - \mathbf{q})$  for  $j = 0, 1, \dots, 5$ . Similarly, we evaluate the truncated Taylor series of  $\Phi_{\nu,h}^e$  which yield

$$W^+ + W_x^+ \xi_j + W_y^+ \eta_j + \frac{1}{2} W_{xx}^+ \xi_j^2 + W_{xy}^+ \xi_j \eta_j + \frac{1}{2} W_{yy}^+ \eta_j^2 = W_j \quad \text{if } \mathbf{P}_j \in \Omega \quad (39)$$

and

$$W^- + W_x^- \xi_j + W_y^- \eta_j + \frac{1}{2} W_{xx}^- \xi_j^2 + W_{xy}^- \xi_j \eta_j + \frac{1}{2} W_{yy}^- \eta_j^2 = W_j \quad \text{if } \mathbf{P}_j \in \Omega^C, \quad (40)$$

where  $W_j \equiv (\Phi_{\nu,h}^e)(\mathbf{p}_j)$  for  $j = 0, 1, \dots, 5$ . Let

$$J_j^i \equiv [V] + [V_x] \xi_j + [V_y] \eta_j + \frac{1}{2} [V_{xx}] \xi_j^2 + [V_{xy}] \xi_j \eta_j + \frac{1}{2} [V_{yy}] \eta_j^2 \quad (41)$$

and

$$J_j^e = [W] + [W_x] \xi_j + [W_y] \eta_j + \frac{1}{2} [W_{xx}] \xi_j^2 + [W_{xy}] \xi_j \eta_j + \frac{1}{2} [W_{yy}] \eta_j^2, \quad (42)$$

for  $j = 0, 1, \dots, 5$ . If the grid node  $p_j \in \Omega^C$ , we rewrite Eq. (38) and Eq. (40) as

$$V^+ + V_x^+ \xi_j + V_y^+ \eta_j + \frac{1}{2} V_{xx}^+ \xi_j^2 + V_{xy}^+ \xi_j \eta_j + \frac{1}{2} V_{yy}^+ \eta_j^2 = V_j + J_j^i \quad \text{if } \mathbf{P}_j \in \Omega^C \quad (43)$$

and

$$W^+ + W_x^+ \xi_j + W_y^+ \eta_j + \frac{1}{2} W_{xx}^+ \xi_j^2 + W_{xy}^+ \xi_j \eta_j + \frac{1}{2} W_{yy}^+ \eta_j^2 = W_j + J_j^e \quad \text{if } \mathbf{P}_j \in \Omega^C. \quad (44)$$

We need to calculate the jumps encountered in Eqs. (41) and (42) at the discretization nodes of the boundary curve  $\partial\Omega$ . Using the values of  $(\xi_j, \eta_j)^T$  and  $(V_j, W_j)^T$  for  $j = 0, 1, \dots, 5$ , we solve the linear system in Eqs. (37) and (43) for  $V^+, V_x^+, V_y^+, V_{xx}^+, V_{xy}^+, V_{yy}^+$  and the linear system in Eqs. (39) and (44) for  $W^+, W_x^+, W_y^+, W_{xx}^+, W_{xy}^+, W_{yy}^+$ , respectively. In the implementation, we usually rewrite the coefficient matrix as independent of the mesh parameter  $h$  by changing  $\xi_j$  to  $\xi_j/h$  and changing  $\eta_j$  to

$\eta_j/h$  for  $j = 0, 1, \dots, 5$ . In the case of the two-dimensional space, if we choose the six grid nodes  $\mathbf{P}_j$  ( $j = 0, 1, \dots, 5$ ) appropriately, *e.g.*, the nearest six grid nodes in a structured grid, the limit values of the solution  $\mathbf{u}_{\nu,h}$  and its derivatives are uniquely determined. As shown in Fig. 2, we choose the nearest ten grid nodes in the structured grid as a ten-point interpolation stencil in the three-dimensional space.

## 6 Algorithm Summary

In this section, we summary the algorithm with emphasis on numerically solving the diffusion part of the bidomain equations by the KFBI method. After choosing the appropriate operator splitting technique and temporal discretization scheme, we present the procedure of solving the BVP defined in Eq.(8) or Eq.(9) with homogeneous Neumann boundary condition by the simple Richardson iteration 1 from  $t^n$  to  $t^{n+1}$ .

---

### Algorithm 1: the KFBI method

---

Denote . Give an initial guess as  $\psi_\nu = 0$  ( $\nu = 0$ ) where  $\nu$  is the iteration number of the simple Richardson iteration.

Denote

$$\mathbf{r} = \mathbf{g}^N - \mathbf{n}_p \cdot \mathbf{D}\nabla_p \left( \int_\Omega G(\mathbf{q}; \mathbf{p}) \mathbf{f}(\mathbf{q}) d\mathbf{q} \right) - \left( \frac{1}{2} \psi(\mathbf{p}) - \int_{\partial\Omega} \mathbf{n}_p \cdot \mathbf{D}\nabla_p G(\mathbf{q}; \mathbf{p}) \psi(\mathbf{q}) ds_{\mathbf{q}} \right)$$

the residual.

Volume integral:

- Get the volume integral  $\mathbf{u}_{h,V}$  from solving the interface problem (17) by an FFT based Poisson solver.
- Compute the limit values of the volume integral

$$\frac{\partial \mathbf{u}_{h,V}^+}{\partial \mathbf{n}} = \mathbf{n}_p \cdot \mathbf{D}\nabla_p \left( \int_\Omega G(\mathbf{q}; \mathbf{p}) \mathbf{f}(\mathbf{q}) d\mathbf{q} \right)$$

at the discretization nodes of the boundary curve by quadratic interpolation.

**while**  $\|\mathbf{r}\| > tol_{Richardson}$  **do**

Boundary integral:

- Evaluate the jumps of the function and its partial derivatives at the intersections to modify the right hand side of the discrete linear system (30) of the equivalent interface problem.
- Get the boundary integral  $\mathbf{u}_{h,B}$  from solving the interface problem (18) by an FFT based Poisson solver.
- Compute the limit values of the boundary integral

$$\frac{\partial \mathbf{u}_{h,B}^+}{\partial \mathbf{n}} = \frac{1}{2} \psi(\mathbf{p}) - \int_{\partial\Omega} \mathbf{n}_p \cdot \mathbf{D}\nabla_p G(\mathbf{q}; \mathbf{p}) \psi(\mathbf{q}) ds_{\mathbf{q}}$$

at the discretization nodes of the boundary curve by quadratic interpolation.

Compute the norm of the residual  $\mathbf{r}$ .

Update the solution  $\mathbf{u}_{\nu,h}^{n+1} \leftarrow \mathbf{u}_{h,V} + \mathbf{u}_{h,B}$ .

Update the iteration number  $\nu \leftarrow \nu + 1$ .

Accept the solution  $\mathbf{u}_{\nu,h}^{n+1}$  as an approximation of the vector function  $\mathbf{u}$  at time  $t = t^{n+1}$ .

---

In the implementation, we first discretize the domain boundary  $\partial\Omega$  by a set of quasi-uniformly spaced nodes and compute the normals, tangents, and curvatures of the curve or the surface at the discretization nodes of the domain boundary. We then partition the larger regular domain  $\mathcal{B}$  into a uniform Cartesian grid and identify the regular and irregular grid nodes. Locate all intersections of the interface with the Cartesian grid lines and compute the unit normals and tangents at those intersections too. All the

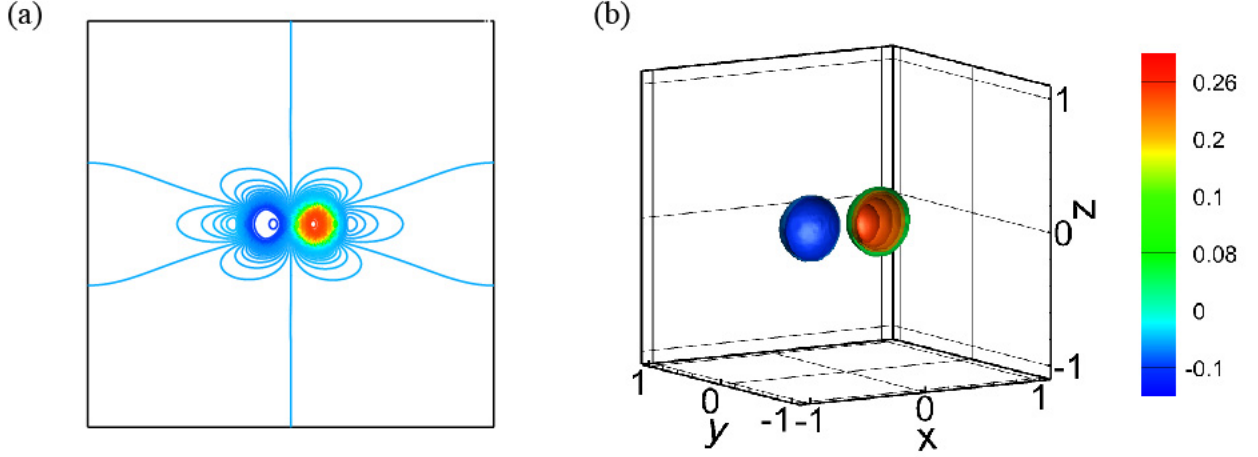


Figure 3: Extracellular stimulus expressed as a virtual electrode which consists of an anode and a cathode (a) in two-dimensional space and (b) in three-dimensional space, respectively.

above information is useful when computing the jumps of the function and its partial derivatives at the intersections and the discretization nodes of the domain boundary. Since the BIE (13) to be solved can be noted as  $\mathcal{A}\psi = \mathbf{g}$ , the simple Richardson iteration method shown in detailed algorithm 1 is easily extended to the GMRES iteration.

## 7 Numerical examples

In this section, we present the numerical results from the KFBI method in different computational domains whose domain boundaries are represented by a set of  $M_{\partial\Omega}$  quasi-uniform spaced nodes. Set the larger regular domain  $\mathcal{B}$  as a square or a cube which is partitioned into a uniform Cartesian grid and denote  $h$  as the mesh parameter. The transmembrane polarization is induced by the application of a virtual electrode consisting of a virtual cathode and a virtual anode [2] and is given by

$$I_{\text{stim}}(\mathbf{x}) = \begin{cases} V_{\text{stim}}^m & \text{if } r < 0.25, \\ -V_{\text{stim}}^m & \text{if } s < 0.25, \end{cases}$$

where  $V_{\text{stim}}^m$  is a constant,  $r$  is the distance between  $\mathbf{x}$  and the anode, and  $s$  is the distance between  $\mathbf{x}$  and the cathode. A depolarization after the application of the virtual battery in two- and three- dimensional spaces are shown in Fig. 3.

In this work, we use the simple but widely used FitzHugh-Nagumo (FHN) model as the membrane dynamics which has one gating variable and is governed by

$$I_{\text{ion}}(V_m, q) = H (q - V_m(V_m - \theta)(1 - V_m)),$$

and

$$\mathcal{M}(V_m, q) = \alpha V_m - \zeta q,$$

where  $H = 100$ ,  $\theta = 0.25$ ,  $\alpha = 5/20$ , and  $\zeta = 1$ . The gating variable  $q$  and the transmembrane voltage  $V_m$  are set to be at rest at time  $t = 0$ . We model the larger regular domain  $\mathcal{B}$  as consisting of fibers that lie parallel to the  $x$ -axis.

For all the numerical simulations, the membrane capacitance per unit area, the surface-to-volume ratio, and the value of the extracellular stimulus are set as  $C_m = 1$ ,  $\beta = 1000$ , and  $V_{\text{stim}}^m = 10$ , respectively. The relative tolerances of the simple Richardson iteration and the GMRES iteration are chosen to be  $10^{-8}$  and the iteration parameter  $\gamma$  for the simple Richardson iteration is selected as 0.8. The positions of the cathode and anode are set as  $(\pm 0.3, 0)$  in two-dimensional space and  $(\pm 0.3, 0, 0)$  in three-dimensional space, respectively. The absolute tolerance in the Newton iteration method for solving the nonlinear systems (3) and (5) is chosen to be  $10^{-10}$ . In all numerical experiments, set the timestep size is the same as the mesh parameter, *i.e.*,  $\Delta t = h$ . The simulations of the bidomain equations are implemented with custom codes written in C++ and the numerical simulations are all performed on a 3.6 GHz computer with an Intel Core i3-4160 CPU.

In two-dimensional space, the bidomain equations are numerically simulated on a circular domain and a heart-shaped domain whose boundaries are presented by a set of quasi-uniformly distributed nodes and the periodic cubic splines on these points. In three-dimensional space, we only use the information of the discrete triangle grid of the domain boundary to simulate the bidomain equations by constructing local coordinate systems, instead of knowing the implicit expression of the domain boundary. In this work, we solve the FHN bidomain equations in a spherical region. The numerical results of the bidomain equations simulated on a human LV space model are shown to demonstrate that the KFBI method works well for complex domains.

We first show the second-order convergence of the KFBI method. In two-dimensional space, we take the solution of the bidomain equation from the KFBI method simulated on a  $2048 \times 2048$  Cartesian grid with  $M_{\partial\Omega} = 2048$  as the high precision solution. To numerically verify the second-order convergence of the KFBI method where a center finite difference method is applied, we estimate the following quality

$$\rho = \frac{\log(e_1/e_2)}{\log(h_1/h_2)}, \quad (45)$$

where  $h_1$  and  $h_2$  are two consecutive mesh parameters and  $e_1$  and  $e_2$  are the corresponding errors in the scaled  $l^2$ -norm or the infinity norm. Here, the scaled discrete  $l^2$ -norm of a vector  $\mathbf{v} = (v_0, v_1, \dots, v_n)^T \in \mathbb{R}^n$  is defined by

$$\|\mathbf{v}\|_{l^2} \equiv \sqrt{\frac{1}{n} \sum_{i=1}^n v_i^2}. \quad (46)$$

As shown in Tables 1-4 and Tables 5-8, in two-dimensional space, the KFBI method has a second-order convergence obtained from the results solved on a circular domain and a heart-shaped domain. In three-dimensional space, we take the solution of the bidomain equation from the KFBI method simulated on a  $512 \times 512 \times 512$  Cartesian grid with  $M_{\partial\Omega} = 2052$  as the high precision solution. As shown in Tables 9-11, the numerical results demonstrate that the KFBI can also achieve a second-order convergence in three-dimensional space, which agree with our expectations well. In Tables 4 and 8, the last two columns show the average iteration numbers of the GMRES iteration in each timestep and the total CPU times (in seconds) at time  $t = 2$ .

We then give the membrane voltage  $V_m$  simulated from the KFBI method on a  $256 \times 256$  and  $128 \times 128$  Cartesian grid, respectively. Figs. 4 and 6 show the contours for the transmembrane voltage  $V_m$  on different computational domains. The transmembrane voltage at discrete times after the application of the virtual battery in a sphere domain are shown in Fig. 8. The trajectories of the transmembrane voltage collected at different points and the iteration number of the GMRES iteration or the simple Richardson iteration are shown.

We finally show the numerical results simulated on a real human LV model which was constructed from an vivo magnetic resonance imaging study of a healthy volunteer [36]. As shown in Fig. , we only need the information of the discretization nodes in the discrete triangle grid of the domain boundary. As shown in Fig. 11, we stimulate one corner of the LV model at the very beginning without applying

$M_{\partial\Omega}$	Grid Size	$\ e_h\ _{l^2}$	$\rho$	$\ e_h\ _{\infty}$	$\rho$
64	64×64	0.063262	-	0.663016	-
128	128×128	0.016879	1.91	0.209426	1.66
256	256×256	0.004422	1.93	0.061362	1.77
512	512×512	0.001150	1.94	0.015737	1.96
1024	1024×1024	0.000313	1.88	0.004245	1.89

Table 1: Errors of the transmembrane voltage in the scaled discrete  $l^2$ -norm and infinity norm solved on the circular domain at time  $t=0.5$ .

$M_{\partial\Omega}$	Grid Size	$\ e_h\ _{l^2}$	$\rho$	$\ e_h\ _{\infty}$	$\rho$
64	64×64	0.156928	-	0.892311	-
128	128×128	0.037347	2.07	0.371083	-
256	256×256	0.008594	2.12	0.092505	2.00
512	512×512	0.002115	2.02	0.022442	2.04
1024	1024×1024	0.000510	2.05	0.005078	2.14

Table 2: Errors of the transmembrane voltage in the scaled discrete  $l^2$ -norm and infinity norm solved on the circular domain at time  $t=1$ .

$M_{\partial\Omega}$	Grid Size	$\ e_h\ _{l^2}$	$\rho$	$\ e_h\ _{\infty}$	$\rho$
64	64×64	0.243811	-	0.943763	-
128	128×128	0.062995	1.95	0.550973	-
256	256×256	0.013931	2.18	0.127781	2.11
512	512×512	0.003317	2.07	0.030559	2.06
1024	1024×1024	0.000734	2.18	0.006604	2.21

Table 3: Errors of the transmembrane voltage in the scaled discrete  $l^2$ -norm and infinity norm solved on the circular domain at time  $t=1.5$ .

any extracellular stimulus and the numerical results demonstrate that the KFBI method works in very complex domains as well as in the easy cases. Scroll wave results of the FHN bidomain equation in the LV space model are shown in Fig. 12.

## 7.1 Example 1

In the case of the two-dimensional space, the intracellular conductivities are 30 along the fiber direction and 5 perpendicular to the fiber direction, while the extracellular conductivities are 20 along the fiber direction and 10 perpendicular to the fiber direction, *i.e.*,  $\sigma_i = 30$ ,  $\eta_i = 5$ ,  $\sigma_e = 20$  and  $\eta_e = 10$ . Tables 1-4 and Figs. 4 and 5 show the numerical results simulated on a circular domain, *e.g.*, the convergence order, CPU cost times (seconds), iso-contours of the transmembrane voltage, and the iteration numbers of the GMRES iteration.

## 7.2 Example 2

Simulating the bidomain equation on the heart-shaped domain in the two-dimensional space, the intracellular and extracellular conductivities are the same as noted previously. Tables 5-8 and Figs. 6 and 7 show the numerical results simulated on a circular domain, *e.g.*, the convergence order, CPU cost times (seconds), iso-contours of the transmembrane voltage, and the iteration numbers of the GMRES iteration.

$M_{\partial\Omega}$	Grid Size	$\ e_h\ _{l^2}$	$\rho$	$\ e_h\ _{\infty}$	$\rho$	#GMRES	CPU (s)
64	$64 \times 64$	0.312412	-	0.954275	-	10.03	4.98
128	$128 \times 128$	0.085055	1.88	0.698887	-	9.65	35.70
256	$256 \times 256$	0.018857	2.17	0.184695	1.92	8.94	272.12
512	$512 \times 512$	0.004393	2.10	0.043494	2.09	8.07	2127.33
1024	$1024 \times 1024$	0.000948	2.21	0.009010	2.27	7.27	16696.65

Table 4: Errors of the transmembrane voltage in the scaled discrete  $l^2$ -norm and infinity norm solved on the circular domain at time  $t=2$ .

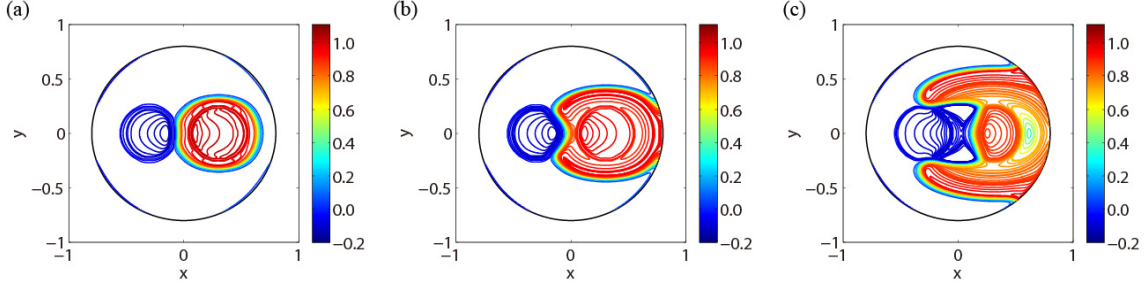


Figure 4: Iso-contours of the transmembrane voltage solved on the circular domain with a  $256 \times 256$  Cartesian grid at time  $t = 0.5$ ,  $t = 1$ , and  $t = 2$ .

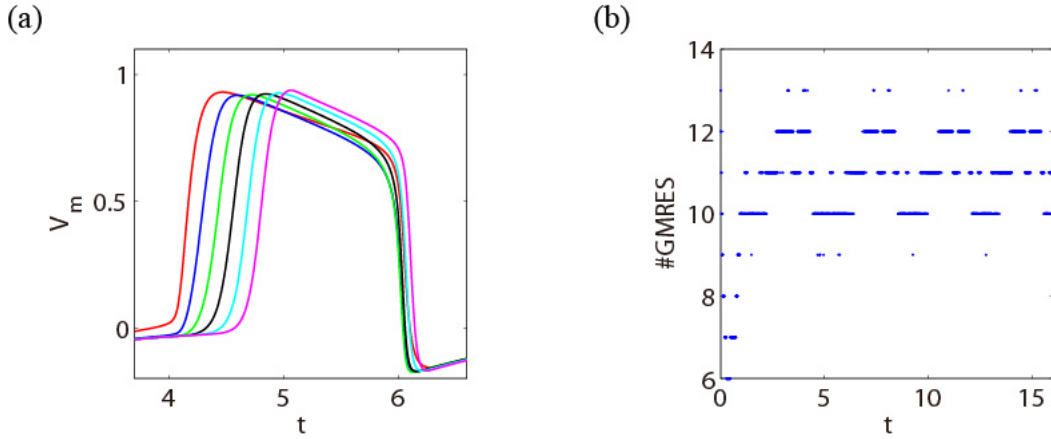


Figure 5: Results of FHN bidomain model on the circular domain with a  $256 \times 256$  Cartesian grid. (a) Trajectories of the transmembrane voltage collected at six points distributed on a straight line from  $(0.5625, 0)$  to  $(0.71875, 0)$  evenly. (b) The iteration number of GMRES iteration against time.

$M_{\partial\Omega}$	Grid Size	$\ e_h\ _{l^2}$	$\rho$	$\ e_h\ _{\infty}$	$\rho$
64	$64 \times 64$	0.068323	-	0.669969	-
128	$128 \times 128$	0.018314	1.90	0.227030	1.56
256	$256 \times 256$	0.004805	1.93	0.062225	1.87
512	$512 \times 512$	0.001253	1.94	0.015830	1.97
1024	$1024 \times 1024$	0.000340	1.88	0.004270	1.89

Table 5: Errors of the transmembrane voltage in the scaled discrete  $l^2$ -norm and infinity norm solved on the heart-shaped domain at time  $t=0.5$ .



$M_{\partial\Omega}$	Grid Size	$\ e_h\ _{l^2}$	$\rho$	$\ e_h\ _{\infty}$	$\rho$
64	64×64	0.169297	-	1.037716	-
128	128×128	0.040869	2.05	0.381248	1.44
256	256×256	0.009457	2.11	0.130960	1.54
512	512×512	0.002317	2.03	0.023010	2.51
1024	1024×1024	0.000544	2.09	0.005196	2.15

Table 6: Errors of the transmembrane voltage in the scaled discrete  $l^2$ -norm and infinity norm solved on the heart-shaped domain at time  $t=1$ .

$M_{\partial\Omega}$	Grid Size	$\ e_h\ _{l^2}$	$\rho$	$\ e_h\ _{\infty}$	$\rho$
64	64×64	0.261088	-	0.950014	-
128	128×128	0.068827	1.92	0.546080	0.80
256	256×256	0.015225	2.18	0.130868	2.06
512	512×512	0.003636	2.07	0.031317	2.06
1024	1024×1024	0.000803	2.18	0.006758	2.21

Table 7: Errors of the transmembrane voltage in the scaled discrete  $l^2$ -norm and infinity norm solved on the heart-shaped domain at time  $t=1.5$ .

$M_{\partial\Omega}$	Grid Size	$\ e_h\ _{l^2}$	$\rho$	$\ e_h\ _{\infty}$	$\rho$	#GMRES	CPU (s)
64	64×64	0.336369	-	0.970956	-	14.23	6.81
128	128×128	0.090293	1.90	0.754806	-	11.36	41.39
256	256×256	0.020045	2.17	0.214061	1.82	12.49	354.83
512	512×512	0.004666	2.10	0.053079	2.01	9.54	2388.28
1024	1024×1024	0.001004	2.22	0.011413	2.22	8.77	19094.92

Table 8: Errors of the transmembrane voltage in the scaled discrete  $l^2$ -norm and infinity norm solved on the heart-shaped domain at time  $t=2$ .

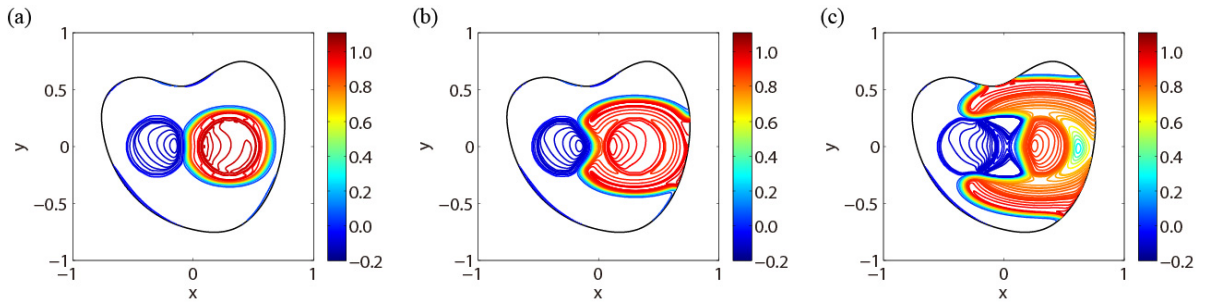


Figure 6: Iso-contours of the transmembrane voltage solved on the heart-shaped domain with a  $256 \times 256$  Cartesian grid at time  $t = 0.5$ ,  $t = 1$  and  $t = 2$ .

### 7.3 Example 3

In this subsection, we show the numerical results of the bidomain equation simulated in a sphere domain. In the case of the three-dimensional case, set the conductivity in the direction orthogonal to the fiber axis be the same as the conductivity in the direction perpendicular to the fiber, *i.e.*,  $\mathbf{D}_i = \text{diag}(30, 5, 5)$  and  $\mathbf{D}_i = \text{diag}(20, 10, 10)$ . Tables 9-11 and Figs. 8 and 9 show the numerical results simulated on a circular domain, *e.g.*, the convergence order, CPU cost times (seconds), iso-contours of the transmembrane

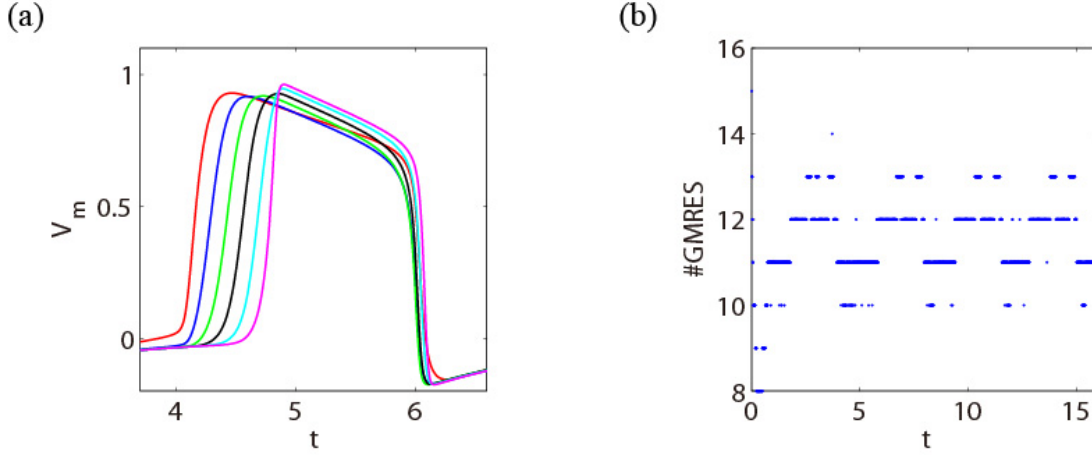


Figure 7: Results of FHN bidomain model on the heart-shaped domain with a  $256 \times 256$  Cartesian grid. (a) Trajectories of the transmembrane voltage collected at six points distributed on a straight line from  $(0.5625, 0)$  to  $(0.71875, 0)$  evenly. (b) The iteration number of GMRES iteration against time.

$M_{\partial\Omega}$	Grid Size	$\ e_h\ _{l^2}$	$\rho$	$\ e_h\ _{\infty}$	$\rho$
18	$32 \times 32 \times 32$	4.16e-02	-	5.25e-01	-
66	$64 \times 64 \times 64$	1.34e-02	1.6	2.12e-01	1.3
258	$128 \times 128 \times 128$	3.04e-03	2.1	7.06e-02	1.6
1026	$256 \times 256 \times 256$	6.20e-04	2.3	2.29e-02	1.6

Table 9: Errors of the transmembrane voltage in the scaled discrete  $l^2$ -norm and infinity norm solved in the spherical region at time  $t=0.25$ .

$M_{\partial\Omega}$	Grid Size	$\ e_h\ _{l^2}$	$\rho$	$\ e_h\ _{\infty}$	$\rho$
18	$32 \times 32 \times 32$	4.52e-02	-	8.00e-01	-
66	$64 \times 64 \times 64$	1.82e-02	1.3	4.92e-01	0.7
258	$128 \times 128 \times 128$	3.16e-03	2.5	1.37e-01	1.8
1026	$256 \times 256 \times 256$	6.11e-04	2.4	2.79e-02	2.3

Table 10: Errors of the transmembrane voltage in the scaled discrete  $l^2$ -norm and infinity norm solved in the spherical region at time  $t=0.5$ .

$M_{\partial\Omega}$	Grid Size	$\ e_h\ _{l^2}$	$\rho$	$\ e_h\ _{\infty}$	$\rho$	#SIMPLE	CPU (s)
18	$32 \times 32 \times 32$	8.69e-02	-	9.11e-01	-	18	22.4
66	$64 \times 64 \times 64$	2.25e-02	1.9	5.13e-01	0.8	19	195.2
258	$128 \times 128 \times 128$	4.30e-03	2.4	1.20e-01	2.1	21	3296.0
1026	$256 \times 256 \times 256$	7.27e-04	2.6	2.49e-02	2.3	16	62291.2

Table 11: Errors of the transmembrane voltage in the scaled discrete  $l^2$ -norm and infinity norm solved in the spherical region at time  $t=0.75$ .

voltage, and the iteration numbers of the simple Richardson iteration.

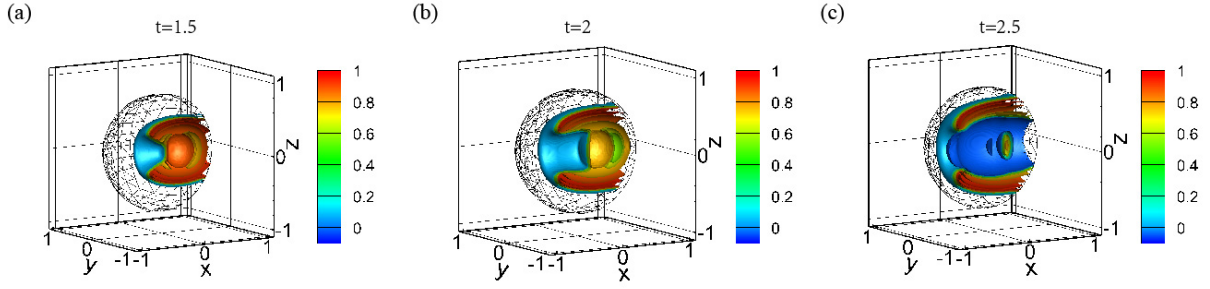


Figure 8: Iso-contours of the transmembrane voltage solved in the spherical region with a  $128 \times 128 \times 128$  Cartesian grid at discrete time  $t = 1.5$ ,  $t = 2$ , and  $t = 2.5$ . The observing domain is limited with  $y \geq 0$ .

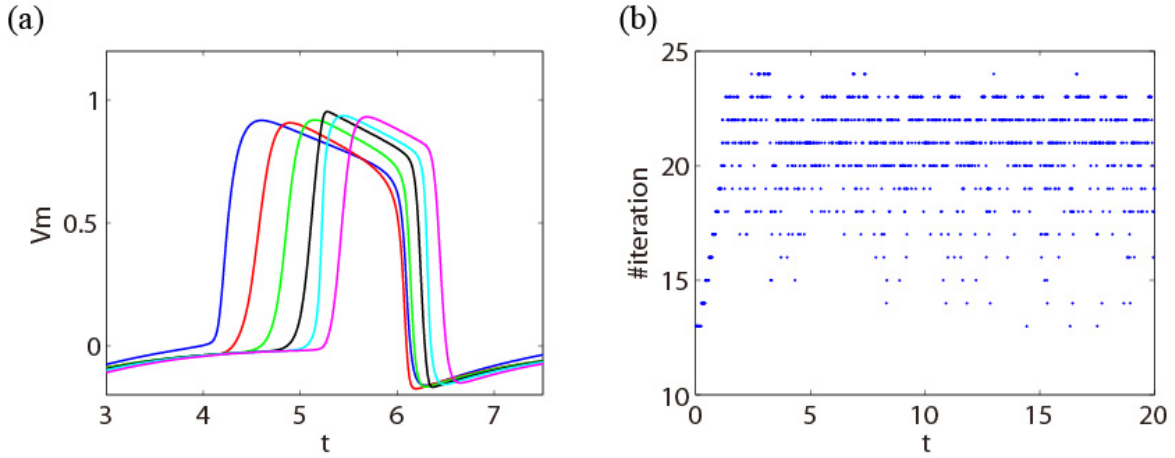


Figure 9: Results of FHN bidomain model in the spherical region with a  $128 \times 128 \times 128$  Cartesian grid. (a) Trajectories of the transmembrane voltage collected at six points distributed on a straight line from  $(0.5625, 0, 0)$  to  $(0.875, 0, 0)$  evenly. (b) The number of the simple Richardson iteration against time and the average iteration number is 21.

#### 7.4 Example 4

We finally simulate the FHN bidomain equations on a LV model which was constructed from an vivo magnetic resonance imaging study of a healthy volunteer [36]. As shown in Fig. 10, in three-dimensional space, we construct local coordinate systems on the discrete triangle grid of the domain boundary to calculate the normals, tangents, and curvatures of the surface at the discretization nodes of the domain boundary. The initial conditions of the transmembrane voltage  $V_m$  and the stage variable  $q$  are given by the smooth data

$$V_m(x, y, z, 0) = \begin{cases} 1 & \text{if } \sqrt{(x - 0.3)^2 + (y - 0.05)^2 + (z - 0.35)^2} < 0.1, \\ 0 & \text{otherwise,} \end{cases}$$

and

$$q(x, y, z, 0) = 0.$$

Set the larger regular domain  $\mathcal{B}$  to be a cube  $[-0.4, 0.4]^3$ . The parameters, tolerances, and modules are set the same as those noted previously in this work except that the iteration parameter  $\gamma$  for the simple

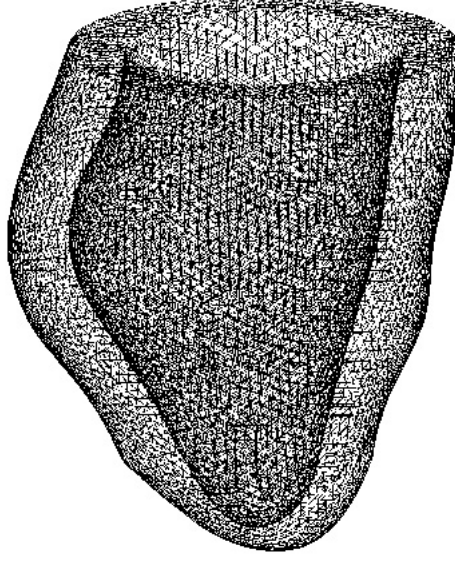


Figure 10: Illustration of the discrete triangle grid of boundary of the LV spatial model.

Richardson iteration method is 0.7. A second stimulus

$$I_s(x, y, z) = \begin{cases} 1 & \text{if } \sqrt{(x - 0.25)^2 + (y - 0.05)^2 + (z - 0.05)^2} < 0.15, \\ 0 & \text{otherwise} \end{cases}$$

is applied to the transmembrane voltage at time  $t = 3.5$ . Figs. 11 and 12 show the traveling waves and scroll wave results simulated on the human LV model.

## 8 Discussion

The bidomain equations which mathematically model the electrical activity of the cardiac tissue are space- and time-dependent problems. In this work, we use the second-order Strang splitting to separate the linear diffusion part from the nonlinear reaction part and integrate the corresponding diffusion equation by the implicit midpoint scheme. The resulting semi-discrete linear diffusion equation which is a homogeneous Neumann boundary value problem can be efficiently solved by the KFBI method without the requirement of the analytical expression of Green's functions. In this work, the KFBI method uses the second-order centered difference method to spatially discrete the equivalent interface problems and uses the quadratic interpolation to calculate the limit values of the integrals at the discretization nodes of the domain boundary. At the same time, the second-order expressions of the domain boundary and a second-order Taylor expansion to compute the jumps of the function and its derivatives across the domain boundary are used in the KFBI method. Numerical results simulated on different domains demonstrate that the KFBI method has second-order accuracy and the iteration number of the simple Richardson iteration and the GMRES iteration is independent of the mesh parameter of the Cartesian grid.

The KFBI method is suitable for the complex computational domains. After embedding the complex computational domain into a larger regular domain, according to the potential theory, the boundary

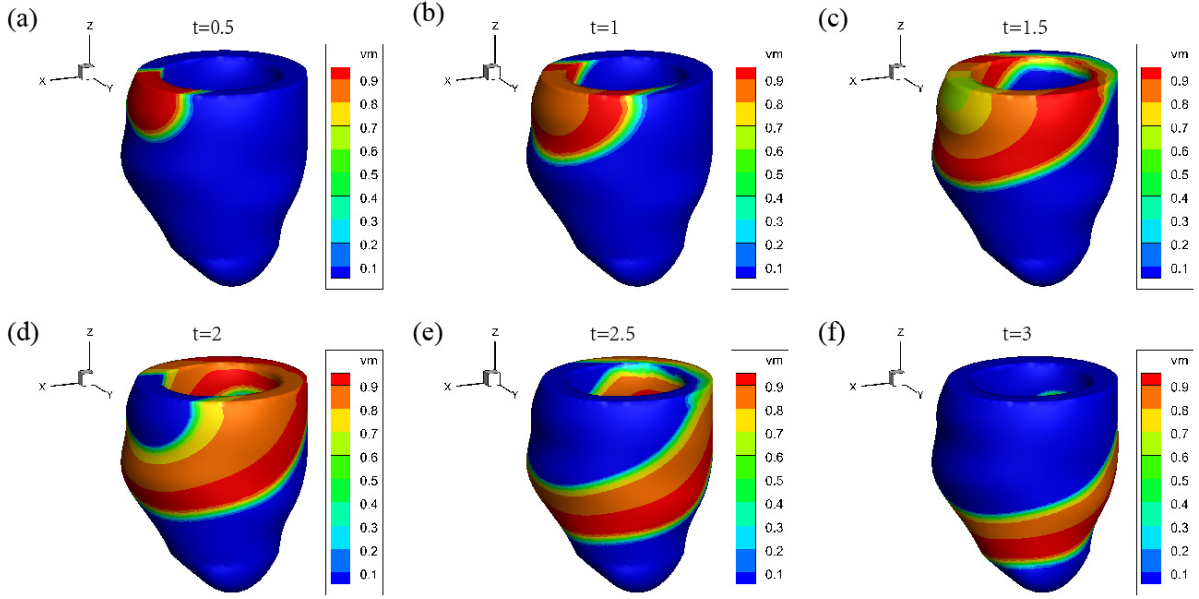


Figure 11: Iso-contours of the transmembrane voltage solved on the human LV model with a  $128 \times 128 \times 128$  Cartesian grid at discrete times.

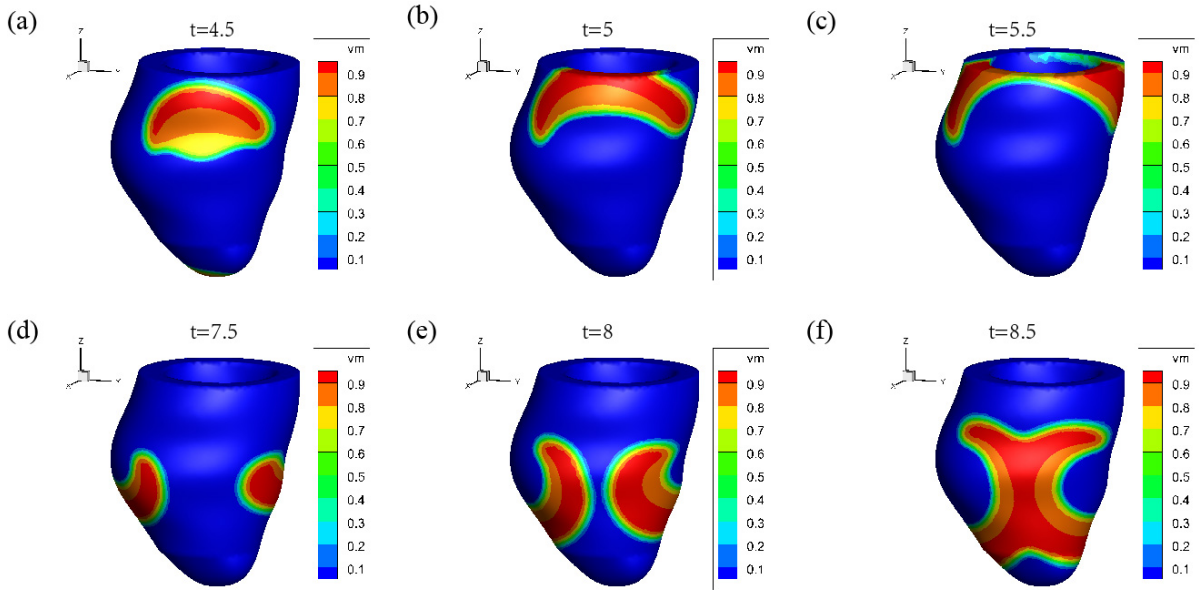


Figure 12: scroll wave results of the FHN bidomain equations simulated on the human LV model.

value problems obtained from the linear diffusion part in the complex computational domain can be reformulated into the second kind of the Fredholm BIEs on the larger regular domain. During each iteration for solving the BIE, the process of solving the equivalent interface problems on the Cartesian grid of the larger regular domain to calculate the corresponding integrals is easy to implement. Moreover, in three-dimensional space, we only need the discrete triangle grid of the domain boundary to estimate the information of the boundary curve by constructing local coordinate systems. The numerical results demonstrate that the KFBI method works well simulating the bidomain equations in a human LV spatial

model. Another advantage of the KFBI method is that the coefficient matrix of the discrete linear system obtained from discretizing the equivalent interface problem is still symmetric and positive definite after appropriate modification at the irregular grid nodes. Therefore, the fast elliptic solvers such as an FFT based Poisson solver can be used to efficiently solve the discrete linear system.

We point out that the KFBI method is not limited to the second-order convergence version which is co-determined by the centered difference method, the quadratic interpolation, the second-order expression of the domain boundary, and the second-order Taylor expansion. The KFBI method can be readily extended to a higher-order version [32, 37] as long as the discrete method and the Taylor expansion involved in the KFBI method are raised to the corresponding order which involves more grid nodes and more Taylor expansion terms.

We emphasize that not only the finite difference method but also the finite element method can be applied for the spatial discretization of the equivalent interface problems. The larger regular domain  $\mathcal{B}$  can be chosen flexibly to be a triangle, a rectangle, a circle, or any other regularly shaped domains as long as the Green's function on  $\mathcal{B}$  exists and the structured grid-based fast elliptic solvers are applicable. Based on the flexibility of the KFBI method, the bidomain equations can be simulated in more general cases, for example, the conductivity is anisotropic and spatially dependent or the computational domain changes over time.

## References

- [1] RH Clayton and AV Panfilov. A guide to modelling cardiac electrical activity in anatomically detailed ventricles. *Progress in biophysics and molecular biology*, 96(1-3):19–43, 2008.
- [2] EJ Vigmond, R Weber Dos Santos, AJ Prassl, M Deo, and G Plank. Solvers for the cardiac bidomain equations. *Progress in biophysics and molecular biology*, 96(1-3):3–18, 2008.
- [3] Rodrigo Weber dos Santos, Gernot Plank, Steffen Bauer, and Edward J Vigmond. Parallel multigrid preconditioner for the cardiac bidomain model. *IEEE Transactions on Biomedical Engineering*, 51(11):1960–1968, 2004.
- [4] Mark Potse, Bruno Dubé, Jacques Richer, Alain Vinet, and Ramesh M Gulrajani. A comparison of monodomain and bidomain reaction-diffusion models for action potential propagation in the human heart. *IEEE Transactions on Biomedical Engineering*, 53(12):2425–2435, 2006.
- [5] Weilun Quan, Steven J Evans, and Harold M Hastings. Efficient integration of a realistic two-dimensional cardiac tissue model by domain decomposition. *IEEE Transactions on Biomedical Engineering*, 45(3):372–385, 1998.
- [6] Nigel F Hooke. Efficient simulation of action potential propagation in a bidomain. 1993.
- [7] Maria Murillo and Xiao-Chuan Cai. A fully implicit parallel algorithm for simulating the non-linear electrical activity of the heart. *Numerical linear algebra with applications*, 11(2-3):261–277, 2004.
- [8] Wenjun Ying, Donald J Rose, and Craig S Henriquez. Efficient fully implicit time integration methods for modeling cardiac dynamics. *IEEE Transactions on Biomedical Engineering*, 55(12):2701–2711, 2008.
- [9] JP Keener and K Bogar. A numerical method for the solution of the bidomain equations in cardiac tissue. *Chaos: An Interdisciplinary Journal of Nonlinear Science*, 8(1):234–241, 1998.
- [10] Zhilin Qu and Alan Garfinkel. An advanced algorithm for solving partial differential equation in cardiac conduction. *IEEE Transactions on Biomedical Engineering*, 46(9):1166–1168, 1999.

- [11] Jonathan P Whiteley. An efficient numerical technique for the solution of the monodomain and bidomain equations. *IEEE Transactions on Biomedical Engineering*, 53(11):2139–2147, 2006.
- [12] Joakim Sundnes, Glenn Terje Lines, and Aslak Tveito. Efficient solution of ordinary differential equations modeling electrical activity in cardiac cells. *Mathematical biosciences*, 172(2):55–72, 2001.
- [13] Andrew E Pollard, Nigel Hooke, and Craig S Henriquez. Cardiac propagation simulation. *Critical reviews in biomedical engineering*, 20(3-4):171–210, 1992.
- [14] Mark L Trew, Bruce H Smaill, David P Bullivant, Peter J Hunter, and Andrew J Pullan. A generalized finite difference method for modeling cardiac electrical activation on arbitrary, irregular computational meshes. *Mathematical biosciences*, 198(2):169–189, 2005.
- [15] G Fischer, B Tilg, R Modre, GJM Huiskamp, J Fetzer, W Rucker, and P Wach. A bidomain model based bem-fem coupling formulation for anisotropic cardiac tissue. *Annals of biomedical engineering*, 28(10):1229–1243, 2000.
- [16] Joakim Sundnes, Glenn Terje Lines, Xing Cai, Bjørn Frederik Nielsen, Kent-Andre Mardal, and Aslak Tveito. *Computing the electrical activity in the heart*, volume 1. Springer Science & Business Media, 2007.
- [17] Natalia Trayanova. Defibrillation of the heart: insights into mechanisms from modelling studies. *Experimental physiology*, 91(2):323–337, 2006.
- [18] Vincent Jacquemet and Craig S Henriquez. Finite volume stiffness matrix for solving anisotropic cardiac propagation in 2-d and 3-d unstructured meshes. *IEEE transactions on biomedical engineering*, 52(8):1490–1492, 2005.
- [19] Mark Trew, Ian Le Grice, Bruce Smaill, and Andrew Pullan. A finite volume method for modeling discontinuous electrical activation in cardiac tissue. *Annals of biomedical engineering*, 33(5):590–602, 2005.
- [20] Anita Mayo. The fast solution of poisson’s and the biharmonic equations on irregular regions. *SIAM Journal on Numerical Analysis*, 21(2):285–299, 1984.
- [21] Anita Mayo. Fast high order accurate solution of laplace’s equation on irregular regions. *SIAM journal on scientific and statistical computing*, 6(1):144–157, 1985.
- [22] Anita Mayo. The rapid evaluation of volume integrals of potential theory on general regions. *Journal of Computational Physics*, 100(2):236–245, 1992.
- [23] Wenjun Ying and Craig S Henriquez. A kernel-free boundary integral method for elliptic boundary value problems. *Journal of computational physics*, 227(2):1046–1074, 2007.
- [24] Wenjun Ying and Wei-Cheng Wang. A kernel-free boundary integral method for variable coefficients elliptic pdes. *Communications in Computational Physics*, 15(4):1108–1140, 2014.
- [25] Youcef Saad and Martin H Schultz. Gmres: A generalized minimal residual algorithm for solving nonsymmetric linear systems. *SIAM Journal on scientific and statistical computing*, 7(3):856–869, 1986.
- [26] James P Keener and James Sneyd. *Mathematical physiology*, volume 1. Springer, 1998.

- [27] John A Trangenstein and Chisup Kim. Operator splitting and adaptive mesh refinement for the Luo-Rudy I model. *Journal of Computational Physics*, 196(2):645–679, 2004.
- [28] Joakim Sundnes. Numerical methods for simulating the electrical activity of the heart. *University of Oslo, Faculty of Mathematics and Natural Sciences*, 1:226, 2002.
- [29] Gerhard Wanner and Ernst Hairer. *Solving ordinary differential equations II*. Springer Berlin Heidelberg, 1996.
- [30] Joakim Sundnes, Glenn Terje Lines, and Aslak Tveito. An operator splitting method for solving the bidomain equations coupled to a volume conductor model for the torso. *Mathematical biosciences*, 194(2):233–248, 2005.
- [31] Yousef Saad. *Iterative methods for sparse linear systems*, volume 82. siam, 2003.
- [32] Yaning Xie and Wenjun Ying. A fourth-order kernel-free boundary integral method for the modified helmholtz equation. *Journal of Scientific Computing*, 78(3):1632–1658, 2019.
- [33] Thomas Beale and Anita Layton. On the accuracy of finite difference methods for elliptic problems with interfaces. *Communications in Applied Mathematics and Computational Science*, 1(1):91–119, 2007.
- [34] Fred W Dorr. The direct solution of the discrete poisson equation on a rectangle. *SIAM review*, 12(2):248–263, 1970.
- [35] Paul N Swarztrauber. The methods of cyclic reduction, fourier analysis and the facr algorithm for the discrete solution of poisson’s equation on a rectangle. *Siam Review*, 19(3):490–501, 1977.
- [36] Li Cai, Hao Gao, Xiaoyu Luo, and Yufeng Nie. Multi-scale modelling of the human left ventricle. *Scientia Sinica Physica, Mechanica and Astronomica*, 45:024702, 01 2015.
- [37] Wenjun Ying. A cartesian grid-based boundary integral method for an elliptic interface problem on closely packed cells. *COMMUNICATIONS IN COMPUTATIONAL PHYSICS*, 24(4):1196–1220, 2018.